FULL PAPER

Ionic Liquid-Assisted Synthesis of TiO$_2$–Carbon Hybrid Nanostructures for Lithium-Ion Batteries

Yanhua Cheng, Zheng Chen, Haobin Wu, Meifang Zhu,* and Yunfeng Lu*

Building nanocomposite architectures based on nanocarbon materials (such as carbon nanotubes and graphene nanosheets) and metal-oxide nanoparticles is of great interests for electrochemical energy storage. Here, an ionic-liquid-assisted strategy is presented to mediate the in situ growth of TiO$_2$ nanocrystals with controlled size on carbon nanotubes and graphene, and also reduce the modified carbon supports to recover the graphitic structure simultaneously. The as-prepared nanocomposites exhibit a highly porous and robust structure with intimate coupling between TiO$_2$ nanocrystals and carbon supports, which offers facile ion and electron transport pathway as well as high mechanical stability. When evaluated as electrode materials for lithium-ion batteries, the nanocomposites manifest high specific capacity, long cycling lifetime, and excellent rate capability, showing their promising application in high-performance energy storage devices.

1. Introduction

Metal oxides are promising candidates for high-capacity anodes in lithium-ion batteries. However, the commercial applications of metal-oxide-based anodes have been limited by their poor ion mobility, electrical conductivity, and structure stability. Hybridizing metal-oxide nanostructures with conductive carbons (e.g., amorphous carbons, carbon nanotubes (CNTs), graphene sheets) in battery electrodes has been widely practiced to overcome the above-mentioned issues.[1,2] Generally, such hybrid materials can simultaneously facilitate ion and electron transport, prevent pulverization of active materials, and ultimately improve the electrochemical energy storage performance.[3]

Metal-oxide–carbon composites with various configurations have been explored as electrode materials.[1,4] For example, amorphous carbon coating on preformed active nanoparticles has been one of the most widely reported architectures of metal-oxide–carbon composites.[5–7] However, tedious procedures are typically involved during the synthesis, and the carbon coating process might cause undesirable reduction of metal oxides. On the other hand, constructing hybrid nanostructures based on metal-oxide particles and graphene/CNT networks have been extensively studied as well.[8–10] In these structures, the 3D interconnected network provides the electrodes with excellent conductivity and mechanical strength, while the intrinsic porosity buffers the volume changes of the active materials. Nevertheless, the hydrophobic nature of carbon and the poor interfacial compatibility between metal oxides and carbon usually make it difficult to fabricate nanocomposites with desirable architecture and strong coupling between two constituents.

Many approaches and techniques have been developed to fabricate metal-oxide–carbon nanocomposites by depositing metal oxides on CNTs/graphene scaffolds (e.g., atomic layer deposition,[11] chemical vapor deposition,[12] and sputtering deposition[13,14] or modifying the surface of carbons (e.g., with surfactants[15–17] or polymers.[18] However, most of these methods suffer from high cost, tedious procedure, and difficulty of scaling up, which make them less attractive for practical production. Recently, there is growing interest in using ionic liquids (ILs) to synthesize metal-oxide nanoparticles[19,20] and to exfoliate carbon materials.[21,22] For example, imidazolium-based IL has been used for the synthesis of highly crystallized metal-oxide nanoparticles with small size[23–25] and for the easy dispersion of carbon nanomaterials via van der Waals interaction.[22,26] These prior researches suggest that IL would be an ideal reaction medium to synthesize carbon–metal-oxide nanocomposites with well controlled architecture and intimate coupled interface.

Herein, we demonstrate the use of an IL (1-ally-3-methylimidazolium chloride, or AmimCl) as a unique reaction medium to direct the growth of metal-oxide nanocrystals (NCs) on CNTs or graphene via a one-pot and additive-free synthesis. Titanium dioxide (TiO$_2$) is chosen as a model metal oxide due to its rich functionality, low cost, and environmentally benignity. As illustrated in **Scheme 1**, the synthesis procedure starts with the dispersion of the carbon constitute (CNTs or graphene oxide) and addition of metal-oxide precursor (i.e., TiCl$_4$) in IL, followed by a simple sol–gel process at low temperature to produce TiO$_2$–carbon nanocomposites. The possible mechanism of forming TiO$_2$–carbon in IL is provided in Supporting Information (Figure S1). Such IL-assisted approach exhibits several advantages, including: (i) easy dispersion of CNTs or

Dr. Y. Cheng, Prof. M. Zhu
State Key Laboratory for Modification of Chemical
Fibers and Polymer Materials
College of Materials Science and Engineering
Donghua University
Shanghai 201620, P. R. China
E-mail: zmf@dhu.edu.cn
Dr. Y. Cheng, Dr. Z. Chen, Dr. H. Wu, Prof. Y. Lu
Department of Chemical and Biomolecular Engineering
University of California
Los Angeles, CA 90095, USA
E-mail: luucla@ucla.edu
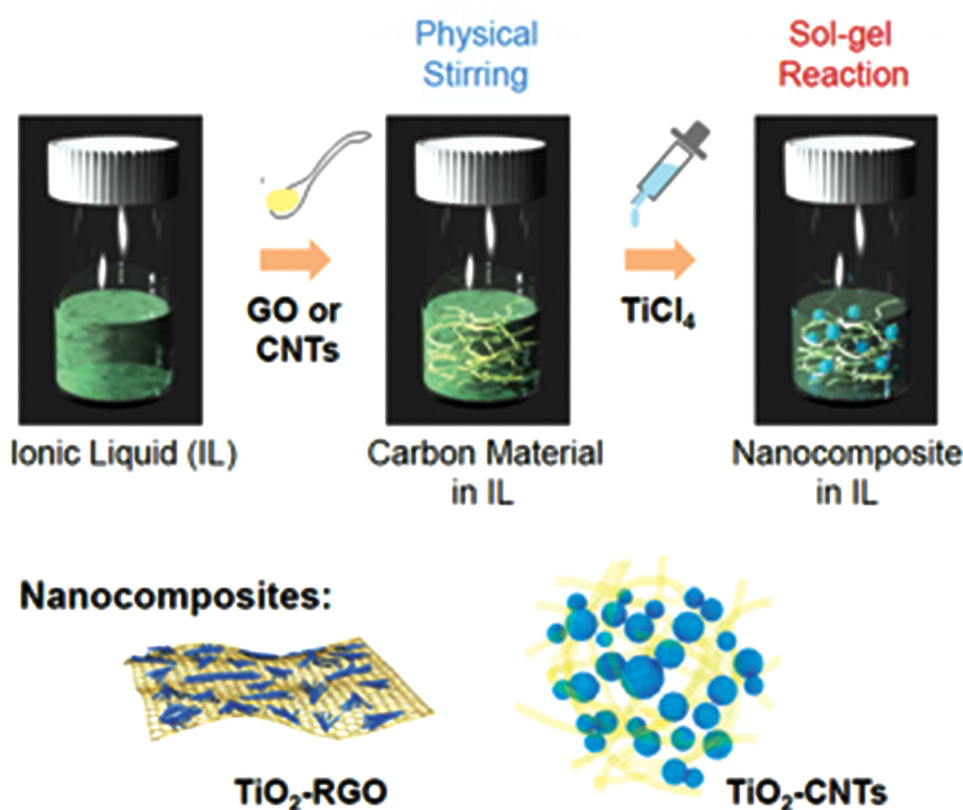
Scheme 1. Schematic illustration for the ionic-liquid-assisted synthesis procedures of TiO$_2$–carbon nanocomposites.

graphene oxide (GO) in IL solution containing TiO$_2$ precursor; (ii) effective restriction of particle size over-growth and aggregation in IL due to the low interface tension of IL; (iii) the IL can directly recover the graphitic structure of carbon (e.g., converting GO into reduced GO (RGO)) without extra reducing agent. During the reaction, the CNTs and GO/RGO act as the supports for the nucleation and growth of TiO$_2$ NCs, ensuring the strong coupling between carbon support and TiO$_2$ NCs. The small particle size of TiO$_2$ NCs minimizes the diffusion distance for both lithium ions and electrons, while the conductive CNTs and RGO framework offers efficient conductive pathway, which together lead to excellent electrode kinetics. The elastic matrix can also buffer the mechanical strain associated with repeated lithium ions insertion/extraction process, giving rise to improved cycling stability. Overall, this work provides a simple but effective synthesis route towards high-performance anode for lithium-ion batteries.

2. Results and Discussion

2.1. Materials Characterizations of the TiO$_2$–RGO and TiO$_2$–CNT Nanocomposites

Figure 1 shows the morphology of the as-prepared TiO$_2$–RGO and TiO$_2$–CNTs nanocomposites. The scanning electron microscopy (SEM) image in Figure 1a,b (at higher magnification) clearly shows that the elongated-shaped TiO$_2$ NCs are uniformly anchored on the RGO sheets after the sol–gel reaction in IL. The planer RGO sheet is covered thoroughly with TiO$_2$ NCs that are lying on the surface of RGO. The simultaneous conversion of GO into RGO can be verified by the color change of the colloidal suspension after reaction (Figure S2, see the Supporting Information).[27,28] Such hybrid structure is also confirmed by transmission electron microscopic (TEM) image as shown in Figure 1c. TiO$_2$ NCs are mostly grown paralleled on the graphene support with a random orientation. The absence of bare RGO and individual TiO$_2$ NCs suggests the strong affinity between these two components. Such intimate contact would guarantee high mechanical robustness and facile electron transport between TiO$_2$ and RGO. It is believed that the IL as reaction mediator could effectively prevent the restacking of RGO[29] and control the nucleation of TiO$_2$ NCs. The TiO$_2$ NCs in the composite are highly crystalline as revealed by the high-resolution TEM image (HRTEM, Figure 1d). The rough surfaces and the lattice fringe of the TiO$_2$ NCs shown in the HRTEM image suggest that the elongated shape might arise from the oriented attachment of primary TiO$_2$ NCs.[30,31]

TiO$_2$–CNTs nanocomposite can also be fabricated based on a similar procedure. SEM image (Figure 1e) shows that the TiO$_2$–CNTs nanocomposite consists of aggregated particles with micrometer size, which are constructed by numerous TiO$_2$ NCs threaded by CNTs (Figure 1f). A closer TEM examination shown in Figure 1g further demonstrates that the CNTs
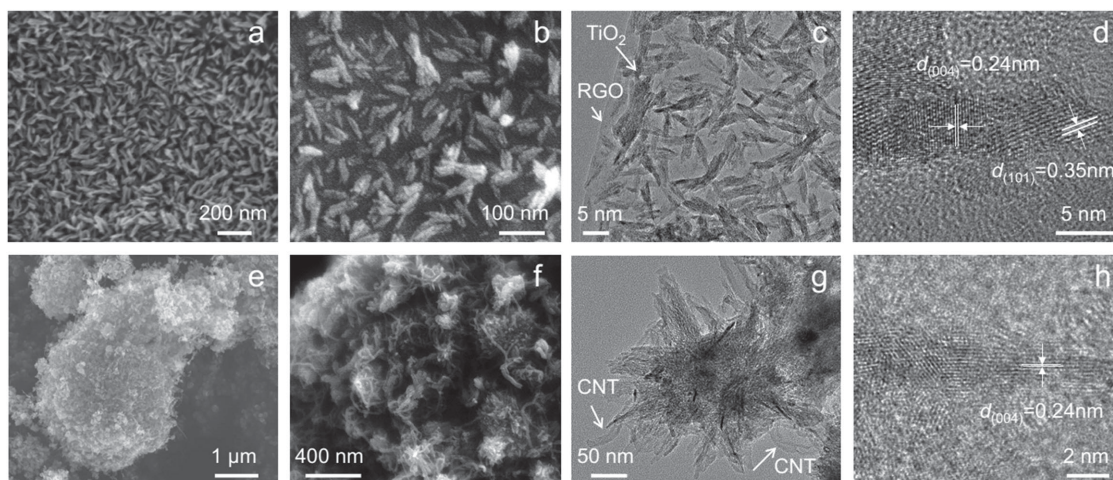
**ADVANCED
FUNCTIONAL
MATERIALS**

www.afm-journal.de

Materials Views

www.MaterialsViews.com

Figure 1. a,b) SEM images and c,d) TEM images of a TiO$_2$–RGO nanocomposite. e,f) SEM images and g,h) TEM images of a TiO$_2$–CNTs nanocomposite.

interpenetrate through clusters of TiO$_2$ NCs without notable phase separation. Consistent with the observation in TiO$_2$–RGO nanocomposite, the TiO$_2$ clusters in TiO$_2$–CNTs nanocomposite are also composed of many small NCs that are attached in an ordered manner as shown in the HRTEM image (Figure 1h).

Figure 2a gives the X-ray diffraction (XRD) pattern of TiO$_2$–RGO nanocomposite, which matches well with that of anatase TiO$_2$.[16] As a reference, the XRD pattern of GO displays a characteristic (002) peak at ≈10°, while pure RGO prepared without TiO$_2$ shows a broad (002) graphene reflection at ≈26°.[32,33] The absence of the (002) peak of GO in the TiO$_2$–RGO nanocomposite suggests that the GO sheets are all converted to RGO and fully covered with TiO$_2$ NCs to prevent possible restacking. Similarly, all the diffraction peaks of TiO$_2$–CNTs nanocomposite can also be indexed to anatase TiO$_2$ (Figure 2b), while the (002) diffraction peak of the CNTs overlaps with the (101) peak of anatase TiO$_2$ and could not be identified. The compositions of the two nanocomposites are determined by thermogravimetric analysis (TGA), with the results shown in Figure 2c. The weight loss at elevated temperature is attributed to the combustion of carbon in the nanocomposites. While tuning the compositions can be easily achieved by adjusting the precursor composition, the content of TiO$_2$ in typical TiO$_2$–RGO and TiO$_2$–CNTs is 84% and 72%, respectively.

X-ray photoelectron spectroscopy (XPS) was further used to determine the chemical nature of the nanocomposites. According to the XPS survey spectrum (Figure S3, see the Supporting Information), both of the nanocomposites mainly contain Ti, O, and C elements. Additionally, a peak at around 400 eV can be seen clearly in both samples, which can be ascribed to N 1s peak.[31] Energy-dispersive X-ray (EDX) mapping images in Figure S4 (see the Supporting Information) further confirm the presence of N in the nanocomposites, which should be derived from IL. The distribution of N element overlaps with that of Ti and O, suggesting the uniform distribution of N in the nanocomposites as a result of strong adsorption of IL on the surface of metal oxides and carbon materials.[34]

Figure 3a shows the C 1s XPS spectrum of GO. The deconvoluted peaks centered at the binding energies of 284.5, 286.5, and 288.0 eV can be assigned to the C—C/C=C, C—O, and C=O functional groups, respectively.[35] In the spectrum of TiO$_2$–RGO (Figure 3b), a dramatic decrease in the carbon-oxygen species is observed, suggesting the partial removal of oxygen-containing functional groups on the carbon support in TiO$_2$–RGO nanocomposite during the reaction, which can be further confirmed by Raman spectroscopy. The Raman spectrum of TiO$_2$–RGO (Figure S5, see the Supporting Information) shows an increase in the intensity ratio of D band
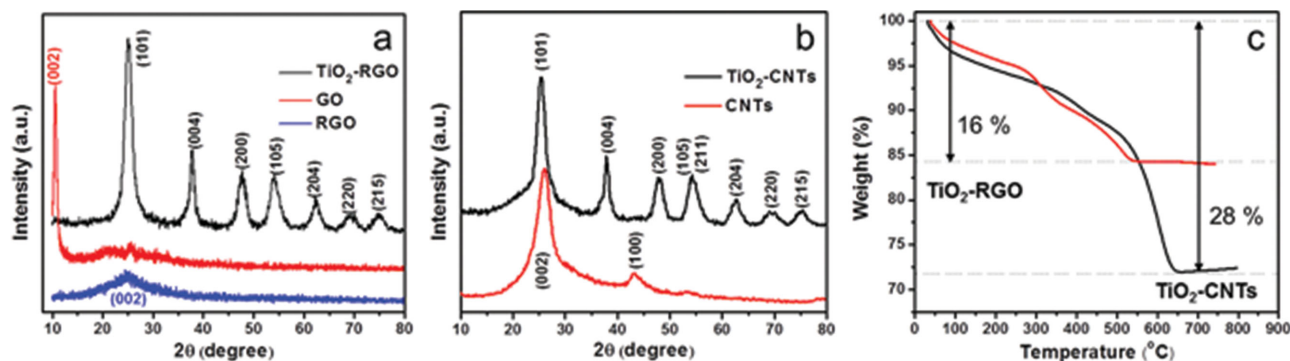

Figure 2. XRD patterns of a) TiO$_2$–RGO nanocomposite, GO, and RGO and b) TiO$_2$–CNTs nanocomposite and CNTs. c) TGA of TiO$_2$–RGO and TiO$_2$–CNTs nanocomposites.
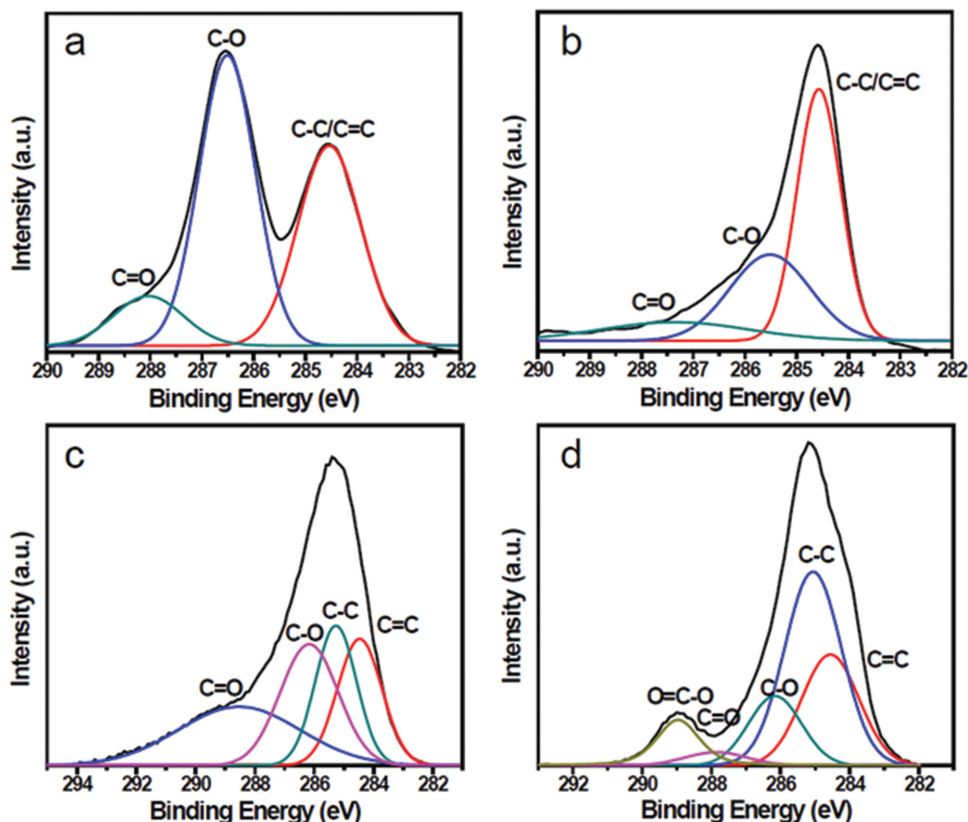
www.MaterialsViews.com

**ADVANCED
FUNCTIONAL
MATERIALS**
www.afm-journal.de

FULL PAPER

Figure 3. The C 1s XPS spectra of a) GO, b) TiO$_2$–RGO nanocomposite, c) oxidized CNTs, and d) TiO$_2$–CNTs nanocomposite.

(located at 1347 cm^{-1}) to G band (located at 1592 cm^{-1}) compared to that of the GO spectrum, which is consistent with previous reports on GO reduction.[36,37] In addition, it is noteworthy that there is a blueshift of G band in the TiO$_2$–RGO compared with that of GO, indicating the interfacial interaction between TiO$_2$ and RGO, further demonstrates a strong coupling between RGO and anatase rather than forming a simple mixture.[38] Similarly, the occurrence of reduction process is found in TiO$_2$–CNTs as well. In Figure 3c, the C1s XPS spectrum of oxidized CNTs clearly indicates a considerable degree of oxidation, which are deconvoluted into C=C (284.5 eV), C—C (285.2 eV), C—O (286.2 eV), and C=O (288.7 eV). The peak intensity of these oxygen-containing functionalities in C 1s XPS spectrum of TiO$_2$–CNTs nanocomposite substantially decreases after reaction (Figure 3d). Similar trend is also observed in C 1s XPS spectrum of pure RGO prepared without TiO$_2$ precursor, again confirming the role of imidazolium-based IL on reducing oxidized carbons (Figure S6, see the Supporting Information).[39] The calculated C/O atomic ratio for RGO is 3.14 in this work, similar to that of hydrazine reduced GO of 3.64,[40] which suggests the effectiveness of reducing GO using the present IL-assisted method.

The porous structures of both nanocomposites were investigated using the nitrogen-sorption technique as shown in **Figure 4**. The pure TiO$_2$ NCs sample (without carbon materials) synthesized in IL displays a mesoporous structure with most of the pores centered at 10 nm (Figure S7, see the Supporting Information). By comparison, the TiO$_2$–RGO and

TiO$_2$–CNTs nanocomposites exhibit more open porous structures due to the incorporation of carbon supports. As a result, the TiO$_2$–RGO and TiO$_2$–CNTs nanocomposites show high Brunauer–Emmett–Teller surface areas of 268 and 176 m^2 g^{-1}, respectively. Meanwhile, the mesopores in both of the nanocomposites have been significantly enlarged as shown in the pore size distribution plots obtained by using the Barrett–Joyner–Halenda (BJH) method (insets of Figure 4). Such highly porous structure provides large interfacial contact with electrolyte, promoted transport kinetics of lithium ions, and effective volume to buffer the strain during the lithium insertion and extraction. The TiO$_2$–CNTs shows the larger and broader pore size distribution in the nanocomposite compared with that of TiO$_2$–RGO, exhibiting a hierarchically porous structure with an open network observed from the SEM and TEM studies (Figure 1e,g), which should be attributed to the rigid and macroporous-structured CNTs (Figure S7, see the Supporting Information). The high conductivity of the carbon support (CNTs and RGO), the intimate interaction between carbon support and TiO$_2$, and the porous structure are expected to enhance the electrochemical performance of the nanocomposites.

2.2. Electrochemical Measurements of TiO$_2$–RGO Nanocomposite

Coin cells were assembled to examine the electrochemical performance of the nanocomposites. The electrochemical
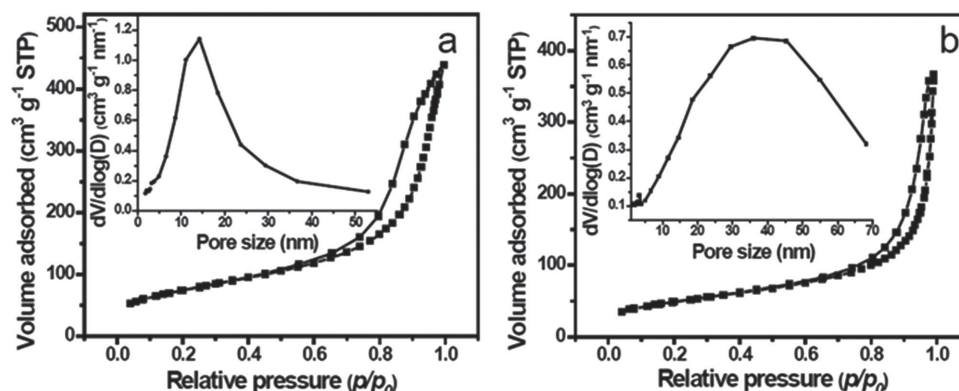
ADVANCED
FUNCTIONAL
MATERIALS
www.afm-journal.de

www.MaterialsViews.com

FULL PAPER

Figure 4. Nitrogen-sorption isotherms of a) TiO_2–RGO and b) TiO_2–CNTs nanocomposite. The insets show the pore-size distribution calculated from desorption branch by BJH method.

behaviors were investigated in two voltage windows of 1.0–3.0 V and 0.005–3.0 V, respectively. **Figure 5**a shows representative cyclic voltammetry (CV) curves of TiO_2–RGO in the voltage range of 1.0–3.0 V at a sweep rate of 0.5 mV s^{-1}. In general, lithium insertion and extraction in anatase TiO_2 electrode can be expressed by the reaction equation $TiO_2 + xLi + e^-$? Li_xTiO_2 ($x = 1$). The theoretical capacity of anatase has been reported as 168 mA h g^{-1} for a fully reversible reaction with $x = 0.5$.[41,42] Two well-defined insertion and extraction peaks are found at 1.7 (cathodic sweep) and 2.0 V (anodic sweep), respectively, indicating the insertion/extraction processes of lithium into/out of the anatase framework. A slight shift of the cathodic peak is observed in the subsequent two cycles due to irreversible reactions, including irreversible replacement of absorbed protons by lithium ions and other electrolyte-related surface reactions.[16] CV measurements at different sweep rates were also performed to evaluate the rate behavior (Figure 5b). As the sweep rate increases, the anodic peak potential shifts to higher voltages and the cathodic peak potential shifts to lower voltages. At the same time, an increase in peak separation is observed. This is due to the increased polarization at higher sweep rates because of kinetic limitations associated with the lithium diffusion through the active material.[43] Although a noticeable peak shift is observed, these current peaks are well retained, suggesting facile electrode kinetics. The CV curves with large symmetric undercurve areas at high sweep rates (e.g., 20 mV s^{-1}) indicate that a significant portion of the charge storage arises from surface reactions.[16] Figure 5c presents a plot of log (i) versus log (v) from 1 to 20 mV s^{-1} for both cathodic and anodic peaks. A linear dependence is observed, suggesting the diffusion-controlled characteristic of the lithium insertion/extraction processes in TiO_2 framework.

Typical galvanostatic charge/discharge curves of TiO_2–RGO nanocomposite electrodes at a current density of 120 mA g^{-1} are shown in Figure 5d. Consistent with the above CV analysis, a distinct voltage plateau is observed for both discharge and charge curves, which indicates coexistence of anatase and lithium titanate phases, similar to that of nanostructured anatase TiO_2 reported previously.[41] A capacity of ≈89 mA h g^{-1} is estimated from this plateau region in the discharge curve, which is controlled by the bulk diffusion of lithium intercalation within the TiO_2 NCs. The slope region mainly accounts

for a surface process with a capacity of about 137 mA h g^{-1}, which is associated with the interfacial lithium storage occurring on small nanoparticles.[42] The dependence of surface-related and diffusion-controlled capacity on the discharge rate is estimated (Figure S8, see the Supporting Information). The surface-related capacity generally remains unchanged at high current densities (≈123 mA h g^{-1}). By comparison, the diffusion-controlled capacity decreases rapidly with increasing current density. Therefore, the contribution of surface-related capacity becomes more dominant at high current density (e.g., ≈55% at 120 mA g^{-1} and 90% at 4800 mA g^{-1}).

To investigate the rate-capability and long-term cycling stability, TiO_2–RGO nanocomposite electrodes were tested at different current densities, followed by continuous cycling at 1200 mA g^{-1} for next 300 cycles. As shown in Figure 5e, TiO_2–RGO nanocomposite shows remarkable capacity of 234 and 174 mA h g^{-1} at high current density of 120 and 1200 mA g^{-1}, respectively. A capacity of 173 mA h g^{-1} can be recovered upon returning back to the current density of 1200 mA g^{-1}. Even after following 300 continuous cycles, a capacity of 154 mA h g^{-1} can still be retained (Figure 5f), suggesting the excellent lithium-storage kinetics and high cycling stability. As a control, a mixture of RGO and TiO_2 NCs with the same mass ratio was prepared and evaluated. Fast capacity decay and poor capacity retention at high current density are observed (Figure S9, see the Supporting Information), which undoubtedly demonstrate the advantages of TiO_2–RGO nanocomposite. Figure S10 (Supporting Information) further compares the performance of the TiO_2–RGO electrodes with several a series of TiO_2 composites.[15,17,44,45] Clearly, as discussed above, the TiO_2–RGO fabricated by in situ IL-assisted strategy outperforms the others. For example, TiO_2–FGS utilized surfactants to facilitate the self-assembly of graphene and in situ grown nanocrystalline TiO_2, which could deliver a capacity of 96 mA h g^{-1} at the rate of 30 C (≈5100 mA g^{-1}).[17] By comparison, TiO_2–RGO used IL as reaction medium in this work, which provides a capacity of 123 mA h g^{-1} even at a higher current density of 7200 mA g^{-1}. The in situ growth of TiO_2 NCs on RGO supports in IL medium is believed to provide robust interface that prevent the separation and loss of contact between these two components, thus offering excellent charge transfer and mechanical stability during long time cycling.
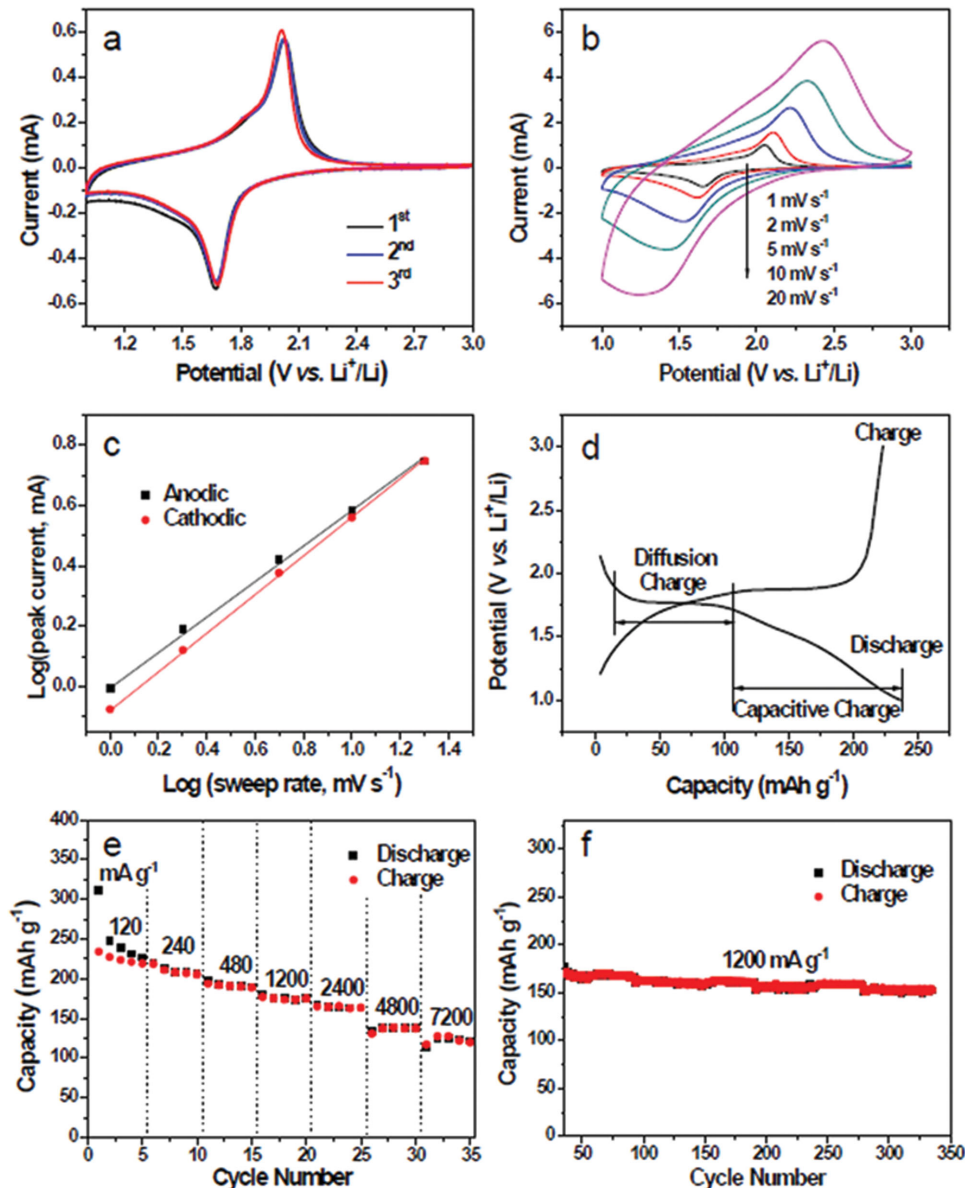
Figure 5. Electrochemical performance of TiO$_2$–RGO nanocomposite in the potential window of 1.0–3.0 V (vs Li$^+$/Li). a) CV plots at the first three cycles at a sweep rate of 0.5 mV s^{-1}. b) CV curves and c) the relationship between log-peak current and log-sweep rate of the electrode from 1 to 20 mV s^{-1}. d) Typical charge/discharge curves at a current density of 120 mA g^{-1}. e) Specific capacity at different current rates and f) cyclic performance at a current density of 1200 mA g^{-1}.

Previous studies indicate that graphene nanosheets are good lithium-storage materials with reversible capacity mainly below 1.0 V versus Li$^+$/Li.[46,47] Thus, the lithium-storage properties of TiO$_2$–RGO nanocomposite were further studied at a wider voltage window between 0.005 and 3.0 V to reveal the possible lithium storage activity of the RGO support. **Figure 6**a shows the CV curves in 0.005–3.0 V, with a similar pair of current peaks at 1.7 and 2.0 V as observed in the range of 1.0–3.0 V. Additionally, a distinct peak appears at low potential approaching 0 V, which can be attributed to the uptake of lithium by RGO.[48] Another peak at around 0.64 V (cathodic sweep) at the first cycle comes from the formation of solid-electrolyte interlayer (SEI).[49] Moreover, the intensity of these redox peaks drops noticeably in

the subsequent scans, indicating the occurrence of irreversible reaction.

Figure 6b shows the galvanostatic charge–discharge profiles at a current density of 60 mA g^{-1}. Clearly, the voltage plateaus of TiO$_2$ are still visible but become less prominent, owing to the presence of the extralong sloping region starting from 0.8 V. A very high capacity of 816 mA h g^{-1} can be delivered for the first discharge, and the corresponding charge capacity only reaches 412 mA h g^{-1}, which indicates a large initial irreversible loss due to the SEI formation. However, the Coulombic efficiency increases significantly to 90% in the subsequent five cycles. As depicted in Figure 6c, the specific discharge capacity of the TiO$_2$–RGO nanocomposite steadily decreases
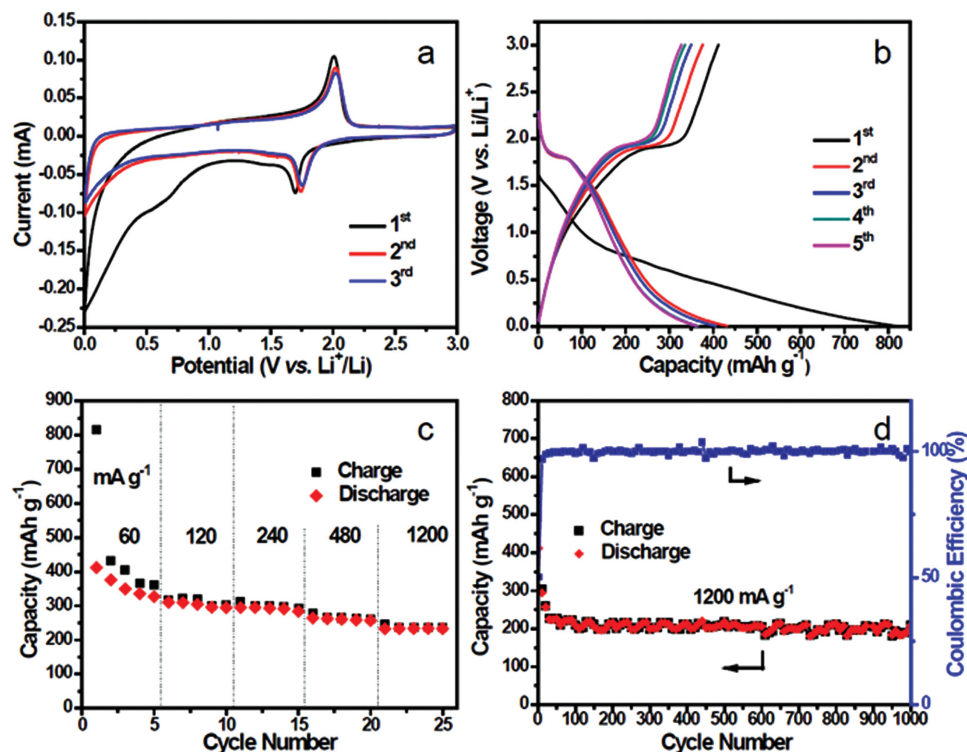
FULL PAPER

Figure 6. Electrochemical performance of TiO_2–RGO nanocomposite in the potential window of 0.005–3.0 V (vs Li⁺/Li). a) CV plots on the first five cycles at a sweep rate of 0.2 mV s⁻¹. b) Charge–discharge voltage profiles at 60 mA g⁻¹. c) Specific capacity at different current densities and d) cyclic performance at a current density of 1200 mA g⁻¹.

from 412 to 232 mA h g⁻¹ when the current density increases from 60 to 1200 mA g⁻¹. Remarkably, the capacity can still be retained at 210 mA h g⁻¹ even after 1000 cycles (90% retention) at a current density of 1200 mA g⁻¹ after the rate performance test (Figure 6d), indicating the excellent stability of the nanocomposite electrodes at low voltage range.

2.3. Electrochemical Measurements of TiO₂–CNTs Nanocomposite

The lithium storage property of TiO_2–CNTs nanocomposite is also investigated. The CV behavior of TiO_2–CNTs at a sweep rate of 0.5 mV s⁻¹ within the voltage range of 1.0–3.0 V is shown in Figure S11a (see the Supporting Information). Similarly, two well-defined current peaks are observed at 1.7 and 2.0 V, respectively, corresponding to lithium insert/extraction processes. Figure S11b (see the Supporting Information) presents the charge/discharge voltage profiles of TiO_2–CNTs nanocomposite at a current density of 60 mA g⁻¹, indicating highly reversible lithium storage property. To investigate the rate-capability and long-term cycling stability, TiO_2–CNTs nanocomposite was tested at different current densities (**Figure 7**a), followed by continuous cycling at 1200 mA g⁻¹ for another 700 cycles (Figure 7b). Discharge capacities of 174, 169, 160, 152, 138, and 125 mA h g⁻¹ are obtained at current densities of 60, 120, 240, 480, 1200, and 2400 mA g⁻¹, respectively. After the next 700 cycles at a current density of 1200 mA g⁻¹, the nanocomposite still delivers a capacity of 136 mA h g⁻¹ without obvious capacity decay.

The lithium-storage properties of the TiO_2–CNTs nanocomposite with a wider voltage window of 0.005–3.0 V were also studied. The CV curves and voltage profiles of TiO_2–CNT nanocomposite are shown in Figure S11c,d (see the Supporting Information), respectively, which are similar to that of TiO_2–RGO. The specific discharge capacity of the TiO_2–CNTs nanocomposite changes from 447 to 251 mA h g⁻¹ when the current density increases from 60 to 1200 mA g⁻¹ (Figure 7c). Such rate capability is remarkable, and comparable or even better than reported TiO_2–CNTs electrodes with different TiO_2 architectures on CNTs.[48,50] After the rate performance test, the electrode retains a stable capacity of 321 mA h g⁻¹ at a current density of 240 mA g⁻¹ for 100 cycles (Figure 7d), suggesting excellent electrode stability.

Similarly, control experiment was also performed using mixture of CNTs and TiO_2 NCs with same mass ratio as that of TiO_2–CNTs nanocomposite (Figure S12, see the Supporting Information). As expected, much lower capacities are obtained in both voltage windows of 1.0–3.0 V and 0.005–3.0 V, with unsatisfactory rate capability. The huge difference of the electrochemical performance between the nanocomposites and physical mixtures highlights the significance of the IL-assisted synthesis method developed in this work.

3. Conclusion

In summary, we have successfully demonstrated a one-step IL-assisted approach to fabricate nanocomposites of TiO_2 and various carbon supports for high-performance electrochemical
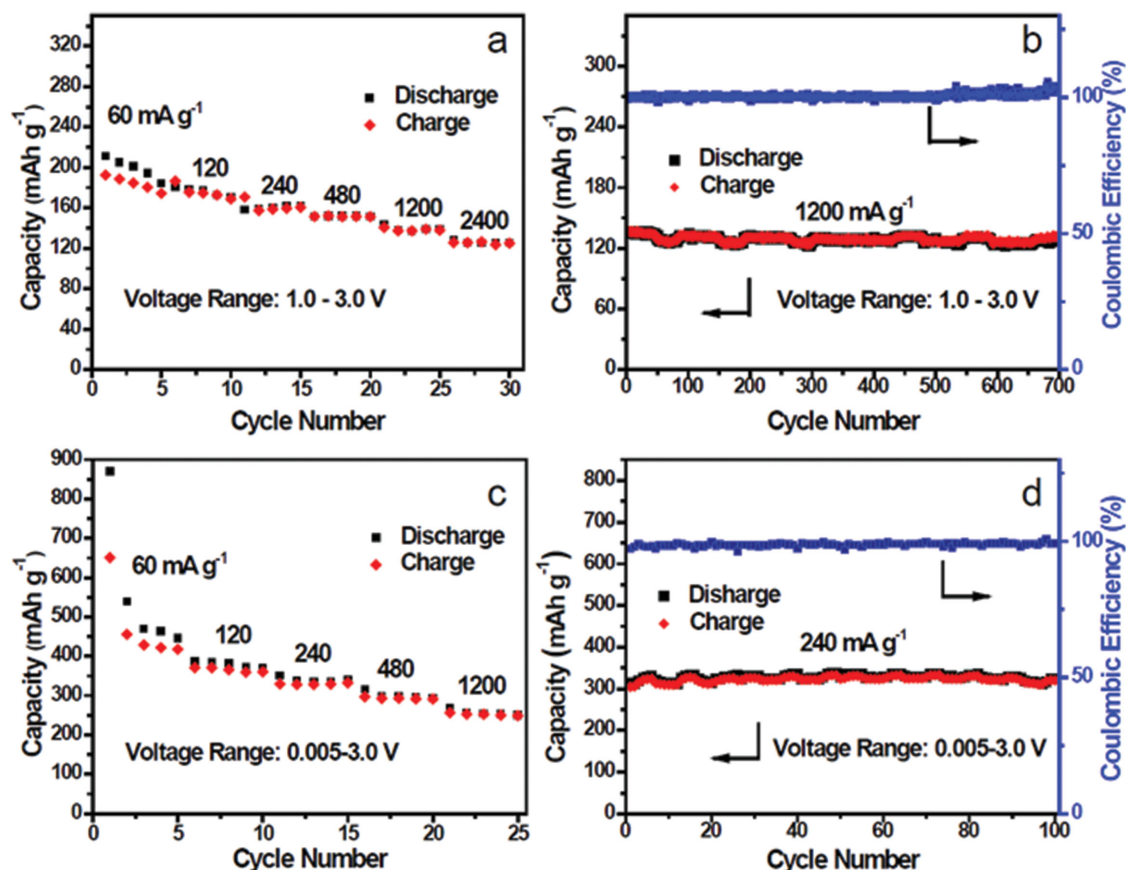
Materials
Views
www.MaterialsViews.com

ADVANCED
FUNCTIONAL
MATERIALS
www.afm-journal.de

FULL PAPER

Figure 7. Electrochemical performance of TiO_2–CNTs nanocomposite. a) Specific capacity at different current rates and b) cyclic performance at a current density of 1200 mA g^{-1} in the potential window of 1.0–3.0 V (vs Li^+/Li). c) Specific capacity at different current rates and d) cyclic performance at a current density of 240 mA g^{-1} in the potential window of 0.005–3.0 V (vs Li^+/Li).

energy storage. The IL plays dual roles in the present strategy, which mediates the uniform growth of TiO_2 NCs on carbons with intimate contact and in situ reduces the modified carbon supports to recover the graphitic structure. The as-prepared nanocomposites exhibit a highly porous and robust structure with strong coupling between TiO_2 NCs and carbon supports, which offers facile ion and electron transport pathway as well as high mechanical stability. As a result, the nanocomposites manifest high specific capacity, long cycling lifetime, and excellent rate capability for electrochemical lithium storage, even at low potential. This work demonstrates a novel IL-based strategy to construct hybrid nanostructures that might benefit a wide range of applications, including chemical sensing, catalysis, and solar cells.

4. Experimental Section

Synthesis of TiO_2–CNTs Nanocomposite: Multiwalled CNTs were oxidized followed by steps in the literature.[51] Briefly, pristine CNTs (12.0 g), HNO_3 (65%, 100 mL), and H_2SO_4 (98%, 300 mL) were mixed in a flask and vigorously stirred under reflux for 100 min. The final product of oxidized CNTs was obtained after washing and drying process. Then, 30 mg of oxidized CNTs were mixed with 2 mL of 1-allyl-3-methylimidazolium chloride (AmimCl) to form uniform black dispersion. 200 µL of $TiCl_4$ was added into the above dispersion to form a high viscous mixture. After slowly adding 400 µL of water

under heavy stirring at room temperature, hydrolysis of $TiCl_4$ occurred immediately followed by the decrease in viscosity. This solution was continuously agitated at 80 °C for 12 h, until precipitates of nanocomposites were completely formed. To collect the product, the obtained dispersion was washed with water, consolidated by centrifugation, and followed by freeze drying.

Synthesis of TiO_2–RGO Nanocomposite: Graphene oxide (GO) was synthesized from natural graphite by a modified Hummer's method. The synthesis process for TiO_2–RGO nanocomposite is similar to that of TiO_2–CNTs, excepting for replacing CNTs with GO. Briefly, 15 mg of GO was added into AmimCl (2 mL), followed by the addition of $TiCl_4$ (200 µL) and water (400 µL). After stirring for 12 h at 80 °C, the product was collected by washing with water, consolidated by centrifugation, and followed by freeze drying.

Synthesis of Pure TiO_2: Pure TiO_2 was synthesized using the same conditions with that of TiO_2–CNTs and TiO_2–RGO, without adding any carbon materials, similar to that described in the literatures.[25,52]

Materials Characterizations: The morphology of TiO_2–CNTs and TiO_2–RGO nanocomposites was investigated by field-emission SEM (FEI Nova 600) and TEM (JEM-2010F). The crystalline structure of the nanocomposites was confirmed by XRD measurements (Rigaku Miniflex II). Raman spectrum was collected using a Renishaw Microscope Raman Spectrometer. TGA was carried out under a flow of air with a temperature ramp of 10 °C min^{-1} from room temperature to 800 °C. Nitrogen sorption isotherms were measured with a Micromeritics ASAP 2020 analyzer. XPS measurements were performed using Thermo ESCALAB 250 spectrometer. Spectra were obtained by irradiating each sample with a 500 µm diameter spot of monochromatic aluminum Ka X-rays at 1486.6 eV.

FULL PAPER

Fabrication of Electrodes: A conventional slurry-coating process was applied to fabricate the electrodes. The active material (TiO_2–CNTs, TiO_2–RGO) powders, carbon black, and poly(vinylidene fluoride) binder were mixed in a mass ratio of 80:5:15 and homogenized in *N*-Methyl-2-pyrrolidone to form slurries. The homogenous slurries were coated on stainless steel substrates and dried at 80 °C for 8 h under vacuum and then annealed at 300 °C for 5 h under N_2. The mass loading was controlled to be 1.5–2 mg cm^{-2} on each current collector.

Electrochemical Measurements: The electrodes were assembled into 2032-type coin cells, using glass fiber (GF/D, Whatman) as separator. Metallic lithium disks were used as counter electrode and 1 M $LiPF_6$ in ethylene carbonate and diethyl carbonate mixture (1:1 by volume) was used as the electrolyte. The CV measurements were carried on a Solartron 1287/1260 Electrochemical Interface. The galvanostatic charge/discharge measurements were performed on LAND CT2000 battery tester at various current densities over voltage ranges of 1.0–3.0 V and 0.005–3.0 V.

Supporting Information

Supporting Information is available from the Wiley Online Library or from the author.

Acknowledgements

[1] L. Zhang, H. B. Wu, X. W. Lou, *Adv. Energy Mater.* **2014**, *4*, DOI: 10.1002/aenm.201300958.

[2] W. Shi, X. Rui, J. Zhu, Q. Yan, *J. Phys. Chem. C* **2012**, *116*, 26685.

[3] S. Goriparti, E. Miele, F. De Angelis, E. Di Fabrizio, R. Proietti Zaccaria, C. Capiglia, *J. Power Sources* **2014**, *257*, 421.

[4] H. B. Wu, J. S. Chen, H. H. Hng, X. Wen Lou, *Nanoscale* **2012**, *4*, 2526.

[5] W. Wang, Q. Sa, J. Chen, Y. Wang, H. Jung, Y. Yin, *ACS Appl. Mater. Interfaces* **2013**, *5*, 6478.

[6] X. W. Lou, C. M. Li, L. A. Archer, *Adv. Mater.* **2009**, *21*, 2536.

[7] H. Sohn, Z. Chen, Y. S. Jung, Q. Xiao, M. Cai, H. Wang, Y. Lu, *J. Mater. Chem. A* **2013**, *1*, 4539.

[8] B. J. Landi, M. J. Ganter, C. D. Cress, R. A. DiLeo, R. P. Raffaelle, *Energy Environ. Sci* **2009**, *2*, 638.

[9] R. Liu, J. Duay, S. B. Lee, *Chem. Commun.* **2011**, *47*, 1384.

[10] M. Pumera, *Energy Environ. Sci.* **2011**, *4*, 668.

[11] J. Luo, J. Liu, Z. Zeng, C. F. Ng, L. Ma, H. Zhang, J. Lin, Z. Shen, H. J. Fan, *Nano Lett.* **2013**, *13*, 6136.

[12] M. D. Lima, S. Fang, X. Lepró, C. Lewis, R. Ovalle-Robles, J. Carretero-González, E. Castillo-Martínez, M. E. Kozlov, J. Oh, N. Rawat, C. S. Haines, M. H. Haque, V. Aare, S. Stoughton, A. A. Zakhidov, R. H. Baughman, *Science* **2011**, *331*, 51.

[13] Y. Wu, Y. Wei, J. Wang, K. Jiang, S. Fan, *Nano Lett.* **2013**, *13*, 818.

[14] C. H. Liu, B. H. Mao, J. Gao, S. Zhang, X. Gao, Z. Liu, S. T. Lee, X. H. Sun, S. D. Wang, *Carbon* **2012**, *50*, 3008.

[15] Z. Chen, D. Zhang, X. Wang, X. Jia, F. Wei, H. Li, Y. Lu, *Adv. Mater.* **2012**, *24*, 2030.

[16] Z. Chen, Y. Yuan, H. Zhou, X. Wang, Z. Gan, F. Wang, Y. Lu, *Adv. Mater.* **2014**, *26*, 339.

[17] D. Wang, D. Choi, J. Li, Z. Yang, Z. Nie, R. Kou, D. Hu, C. Wang, L. V. Saraf, J. Zhang, I. A. Aksay, J. Liu, *ACS Nano* **2009**, *3*, 907.

[18] Y. Cheng, Z. Chen, M. Zhu, Y. Lu, *Adv. Energy Mater.* **2015**, *5*, DOI: 10.1002/aenm.201401207.

[19] W. Zheng, X. Liu, Z. Yan, L. Zhu, *ACS Nano* **2008**, *3*, 115.

[20] M. Antonietti, D. Kuang, B. Smarsly, Y. Zhou, *Angew. Chem., Int. Ed.* **2004**, *43*, 4988.

[21] T. Fukushima, T. Aida, *Chem.-Eur. J.* **2007**, *13*, 5048.

[22] J. Wang, H. Chu, Y. Li, *ACS Nano* **2008**, *2*, 2540.

[23] T. Nakashima, N. Kimizuka, *J. Am. Chem. Soc.* **2003**, *125*, 6386.

[24] K. Ding, Z. Miao, Z. Liu, Z. Zhang, B. Han, G. An, S. Miao, Y. Xie, *J. Am. Chem. Soc.* **2007**, *129*, 6362.

[25] Y. Zhou, M. Antonietti, *J. Am. Chem. Soc.* **2003**, *125*, 14960.

[26] T. Fukushima, A. Kosaka, Y. Ishimura, T. Yamamoto, T. Takigawa, N. Ishii, T. Aida, *Science* **2003**, *300*, 2072.

[27] G. Williams, B. Seger, P. V. Kamat, *ACS Nano* **2008**, *2*, 1487.

[28] H. A. Becerril, J. Mao, Z. Liu, R. M. Stoltenberg, Z. Bao, Y. Chen, *ACS Nano* **2008**, *2*, 463.

[29] Y. Fu, J. Zhang, H. Liu, W. C. Hiscox, Y. Gu, *J. Mater. Chem. A* **2013**, *1*, 2663.

[30] K. Ding, Z. Miao, B. Hu, G. An, Z. Sun, B. Han, Z. Liu, *Langmuir* **2010**, *26*, 10294.

[31] Y. J. He, J. F. Peng, W. Chu, Y. Z. Li, D. G. Tong, *J. Mater. Chem. A* **2014**, *2*, 1721.

[32] S. Ding, D. Luan, F. Y. C. Boey, J. S. Chen, X. W. Lou, *Chem. Commun.* **2011**, *47*, 7155.

[33] H. F. Xiang, Z. D. Li, K. Xie, J. Z. Jiang, J. J. Chen, P. C. Lian, J. S. Wu, Y. Yu, H. H. Wang, *RSC Adv.* **2012**, *2*, 6792.

[34] L. Zhao, Y. S. Hu, H. Li, Z. Wang, L. Chen, *Adv. Mater.* **2011**, *23*, 1385.

[35] T. Kim, H. Lee, J. Kim, K. S. Suh, *ACS Nano* **2010**, *4*, 1612.

[36] I. K. Moon, J. Lee, R. S. Ruoff, H. Lee, *Nat. Commun.* **2010**, *1*, 73.

[37] H. J. Shin, K. K. Kim, A. Benayad, S. M. Yoon, H. K. Park, I. S. Jung, M. H. Jin, H. K. Jeong, J. M. Kim, J. Y. Choi, Y. H. Lee, *Adv. Funct. Mater.* **2009**, *19*, 1987.

[38] J. Yu, T. Ma, S. Liu, *Phys. Chem. Chem. Phys.* **2011**, *13*, 3491.

[39] M. H. G. Prechtl, P. S. Campbell, J. D. Scholten, G. B. Fraser, G. Machado, C. C. Santini, J. Dupont, Y. Chauvin, *Nanoscale* **2010**, *2*, 2601.

[40] S. Dubin, S. Gilje, K. Wang, V. C. Tung, K. Cha, A. S. Hall, J. Farrar, R. Varshneya, Y. Yang, R. B. Kaner, *ACS Nano* **2010**, *4*, 3845.

[41] T. Brezesinski, J. Wang, J. Polleux, B. Dunn, S. H. Tolbert, *J. Am. Chem. Soc.* **2009**, *131*, 1802.

[42] J. Y. Shin, D. Samuelis, J. Maier, *Adv. Funct. Mater.* **2011**, *21*, 3464.

[43] M. Mancini, P. Kubiak, M. Wohlfahrt-Mehrens, R. Marassi, *J. Electrochem. Soc.* **2010**, *157*, A164.

[44] H. Liu, W. Li, D. Shen, D. Zhao, G. Wang, *J. Am. Chem. Soc.* **2015**, *137*, 13161.

[45] Y. Qiu, K. Yan, S. Yang, L. Jin, H. Deng, W. Li, *ACS Nano* **2010**, *4*, 6515.

[46] S. Guo, S. Dong, *Chem. Soc. Rev.* **2011**, *40*, 2644.

[47] Z. S. Wu, W. Ren, L. Xu, F. Li, H. M. Cheng, *ACS Nano* **2011**, *5*, 5463.

[48] S. Ding, J. Chen, X. Lou, *Adv. Funct. Mater.* **2011**, *21*, 4120.

[49] Z. Yang, G. Du, Q. Meng, Z. Guo, X. Yu, Z. Chen, T. Guo, R. Zeng, *J. Mater. Chem.* **2012**, *22*, 5848.

[50] F. F. Cao, Y. G. Guo, S. F. Zheng, X. L. Wu, L. Y. Jiang, R. R. Bi, L. J. Wan, J. Maier, *Chem. Mater.* **2010**, *22*, 1908.

[51] Z. Chen, Y. Qin, D. Weng, Q. Xiao, Y. Peng, X. Wang, H. Li, F. Wei, Y. Lu, *Adv. Funct. Mater.* **2009**, *19*, 3420.

[52] C. Li, L. Gu, J. Tong, J. Maier, *ACS Nano* **2011**, *5*, 2930.